Universität Karlsruhe (TH)
Institut für Baustatik

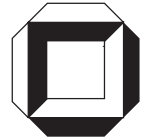# Numerical simulation of DLR-Benchmark: Axially compressed stiffened CFRP panel

W. Wagner

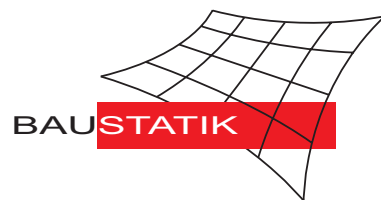Mitteilung 2(2002)

BAUSTATIK

Universität Karlsruhe (TH)
Institut für Baustatik

Numerical simulation of DLR-Benchmark: Axially compressed stiffened CFRP panel

W. Wagner

Mitteilung 2(2002)

Prof. Dr.–Ing. W. Wagner   Telefon: (0721) 608–2280
Institut für Baustatik   Telefax: (0721) 608–6015
ⓒ Universität Karlsruhe   E–mail: bs@.uni-karlsruhe.de
Postfach 6980   Internet: http://www.bs.uni-karlsruhe.de
76128 Karlsruhe

GARTEUR – AG 25

Postbuckling and Collapse Analysis

Numerical simulation of DLR-Benchmark: Axially compressed stiffened CFRP panel

Doc. N^o:	**3-University of Karlsruhe**
Issue:	**3.1**
Date:	**June, 07, 2002**
Benchmark N^o:	**3**

Prepared by: **Prof. Dr.–Ing. habil. W.Wagner**
Institut für Baustatik
Universität Karlsruhe (TH)
Germany

Contents

1 Introduction

Finite element calculations are performed for an axially compressed stiffened CFRP panel. This panel was earlier investigated experimentally by DLR in Braunschweig, Germany. Experimental data are available. The panel consists of a skin with nominally cylindrical shape, which is stiffened by stringers. The stringers are partially separated from the skin. Simulations are performed only for the undamaged panel. The DLR benchmark panel and its tests are described in [3].

Calculations are performed with:

- FE-code: an extended Version of Finite Element Program FEAP, described in [7]
- Computer: DELL C-800 Notebook, 800 MHz Pentium III Mobile, 512 MB RAM,
              operating system Windows 2000 Professional

Units used within all calculations are:

- Length, displacements: mm
- Forces: kN

2 Geometry of the panel, laminate set-up, material properties

The panel, described in [3], is one sixth (60°) of a cylinder of 800 mm height and 400 mm radius, see table 1. At the inner side 6 stringers are applied in axial direction at equal distances (10° angular distance).

Panel length	l	= 800 mm
Free length (maximum buckling length)	l_f	= 620 mm
Radius (nominal value!)	r	= 400 mm
Average of the radii of the panel	r_a	370.9 mm
Arc length	a	= 419 mm
Number of stringers	n	= 6
Distance stringer to stringer	d	= a / 6
Distance stringer to longitudinal edge	e	= d / 2
Laminate set-up of skin		[90, +45, -45, 0]s
Laminate set-up of stringers blade		[(+45, -45)3, 06]s
Ply thickness	t	= 0.125 mm
Stringer height	h	= 14 mm
Stringer width	f	= 37.9 mm

Table 1: Geometrical data of the panel

All laminate layers are unidirectional and made from the same material. The associated material data are depicted in 2, see [3]: The lay-up and the fiber orientation for the stringer are shown in Fig. 1.

3 Loading and constraints

From the experiments it is known that the upper and lower border of the panel are fixed up to a height of 90 mm in stiff clamping boxes, see Fig. 2. The panel is then subjected to a uniform compressing displacement of the upper border resulting from a movement of the upper clamping box.

3

Longitudinal modulus of elasticity (in axial direction of panel)	E_{11}	= 141	kN/mm^2
Transverse modulus of elasticity	E_{22}	= 11	kN/mm^2
In-plane Shear modulus	G_{12}	= 6.29	kN/mm^2
Transverse shear moduli	G_{13}	= 6.29	kN/mm^2
	G_{23}	= 4.29	kN/mm^2
Poisson's ratio	ν	= 0.3	
Material density (not given in [3]/, estimated to)	r	= $1.6 \cdot 10^{-6}$	kg / mm^3

Table 2: Material data of the panel
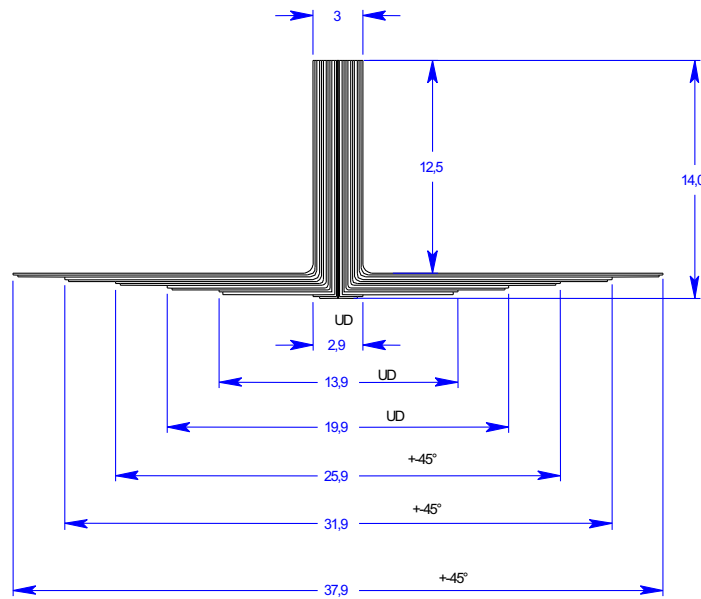
Figure 1: Lay-up of the stringer (from [3])

Lateral supports as shown in Fig. 3 are supplied. They have a height of 600 mm, leaving free distances of 10 mm between their ends and the clamping boxes. The lateral clamping comes to a width of 25 mm, covering not only the skin, but also a part of the flange of the neighbouring stringer (not represented in the figure).

In the numerical model the following boundary constraints have been introduced, see Fig. 4:

Top and bottom (first and second row of nodes): axial displacements are free, horizontal and radial displacements and all rotations are fixed. In addition the axial displacement is fixed at the bottom (first row). At top all nodes are linked in axial direction. Thus, the same displacement is introduced for all nodes. At the lateral edges only radial displacements have been fixed, see Fig. 4. A more realistic type of boundary condition may be that all nodes at the lateral edges are only linked together. This mean that all nodes at the edges have same displacements. This type of boundary condition has been used in some calculations. The test facility and a principal view of the experiment at DLR are presented in Fig. 5.
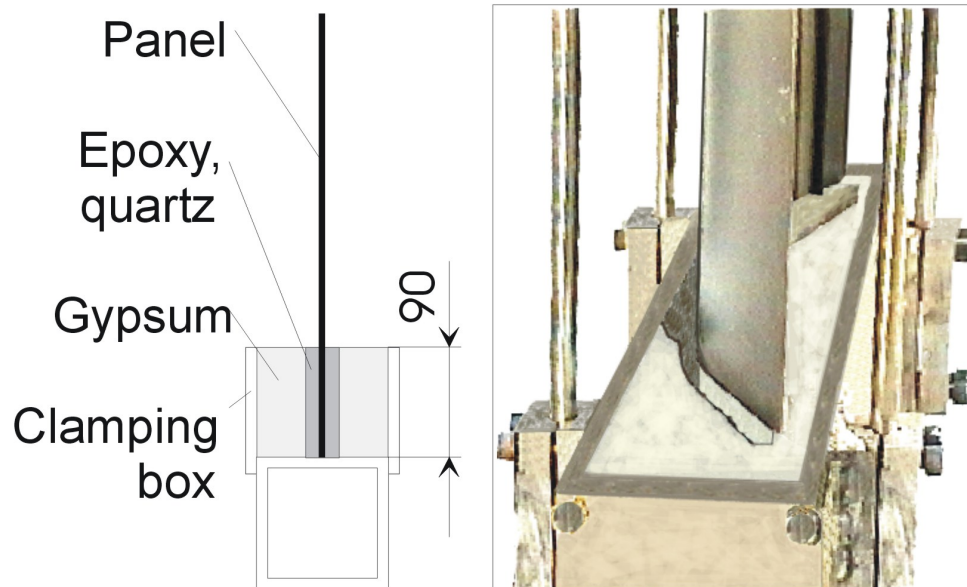
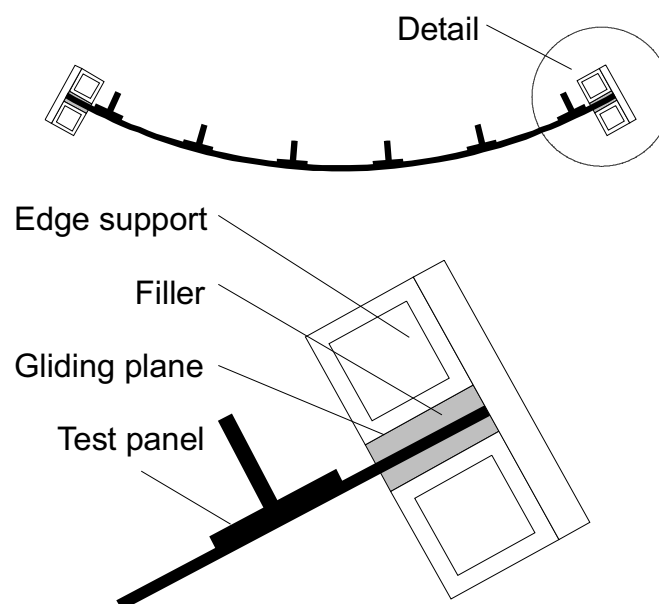Figure 2: Boundary conditions at loaded edges (from [3])

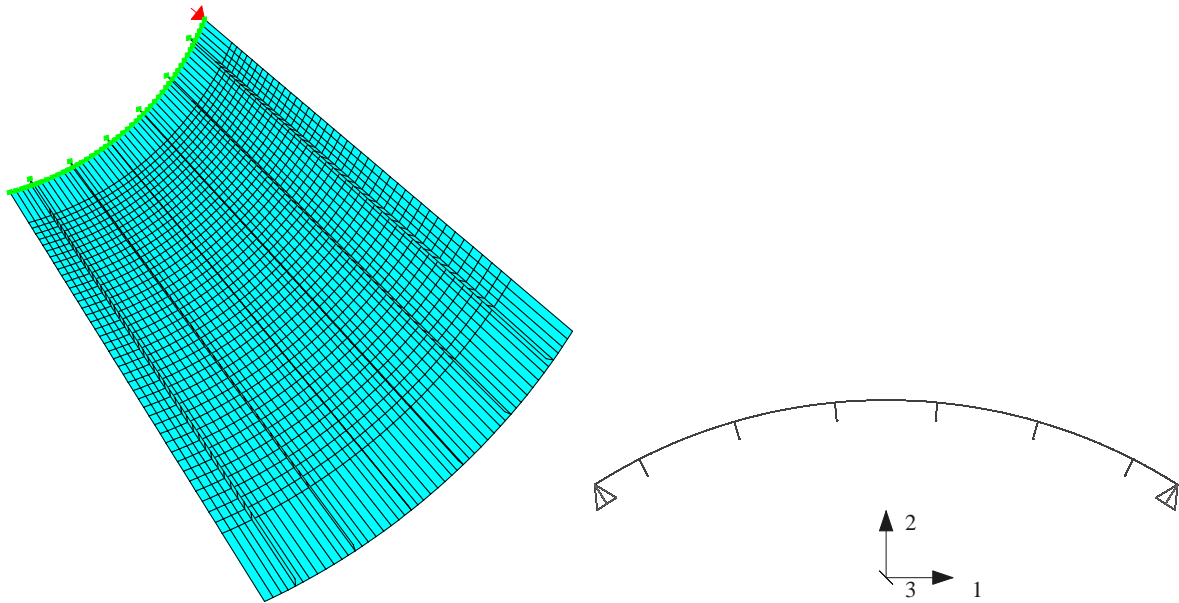Figure 3: Support of the lateral panel edges (from [3])

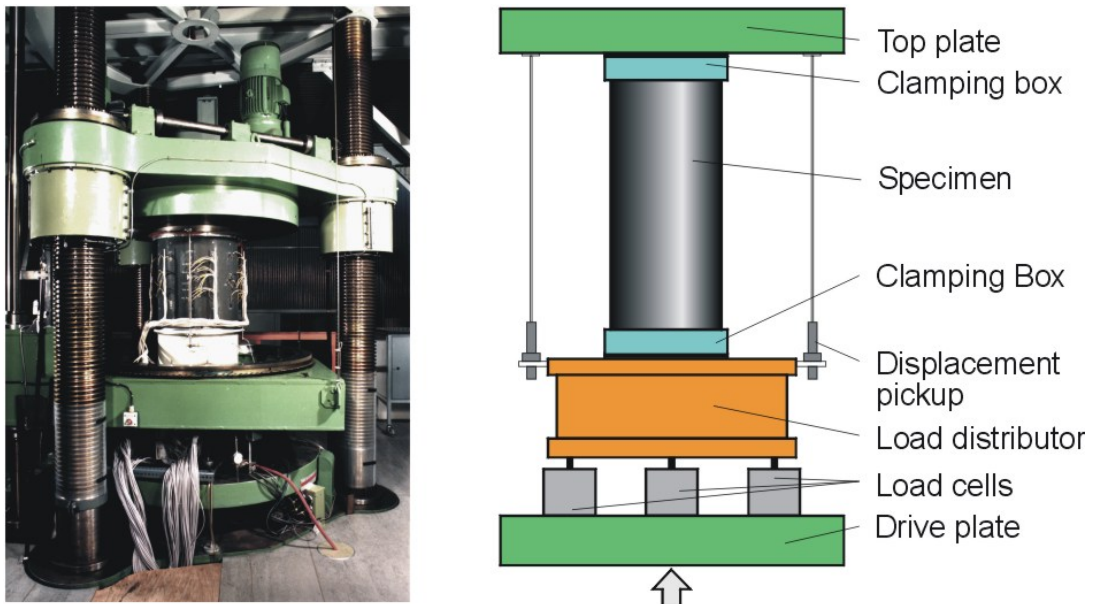Figure 4: FE–mesh of the panel and boundary conditions

Figure 5: Test facility and principal view of the experiment (from [3])

4 FE–modeling

4.1 Elements

Within the numerical analysis two strategies have been introduced . The first one is to use 3D–type elements with a special layer technique, the second one is to use layered thin shell elements.

Hexahedral elements based on standard displacement formulations exhibit a severe locking behaviour, especially if these elements are applied to thin structures. It is well known that the standard isoparametric eight–node element with trilinear shape functions can be essentially improved when applying the assumed strain method (ANS) to some strain components. Following [1] the transverse shear strains of the middle plane are independently interpolated using special shape functions. The thickness strains are approximated considering the approach in [2]. Furthermore, the membrane behaviour is improved by applying the enhanced assumed strain method (EAS) with five or more parameters [4]. A variational formulation and detailed finite element equations of an ANS–EAS5–element can be found in [5].

Shell–elements based on the so–called first order shear deformation theory are quite standard. Concerning theoretical and numerical details for such formulations we refer to the literature. A straight forward formulation where finite rotations are taken into account is described in [6] and has been used in the current analysis. The reference surface of the element can be chosen everywhere. Thus nodes at top or bottom of the element are possible.

Both element formulations have a consistent tangent matrix. Thus quadratic convergence can be achieved within the numerical iterative analysis.

4.2 Material law

In both element formulations an orthotropic material law with linear elastic material behaviour has been used. The lay-up is described within the shell–element in an analytical integration process over the thickness. Within the 3D-element it is possible to summarize some layers in on element or to choose only one layer per element. A numerical integration procedure has to be used. Details of this procedure are described in [5].

4.3 Discretization

4.3.1 Hexahedral element

FE–meshes are introduced with 4-6 elements for the skin between the stringers, which lead to 120 elements in circumferential direction. In vertical directions meshes with 40/60/80 and 90 elements and 2+2 elements for the clamping area are used. Furthermore the stringer blades are discretized with up to 4 elements. Meshes can be seen in Fig. 6. The reference surface is the mid–surface of the skin. No imperfections have been used. The damaged areas are not discretized. The radius of the mid–surface of the cylindrical skin has been chosen to r = 370.9 mm according to [3]. The influence of different numbers of elements in vertical direction has been studied. Results for associated critical loads within a nonlinear analysis are depicted in Fig. 7. In total 4 different discretization models for the stringers have been used, see Fig. 8. The associated FE–meshes are described in Table 3
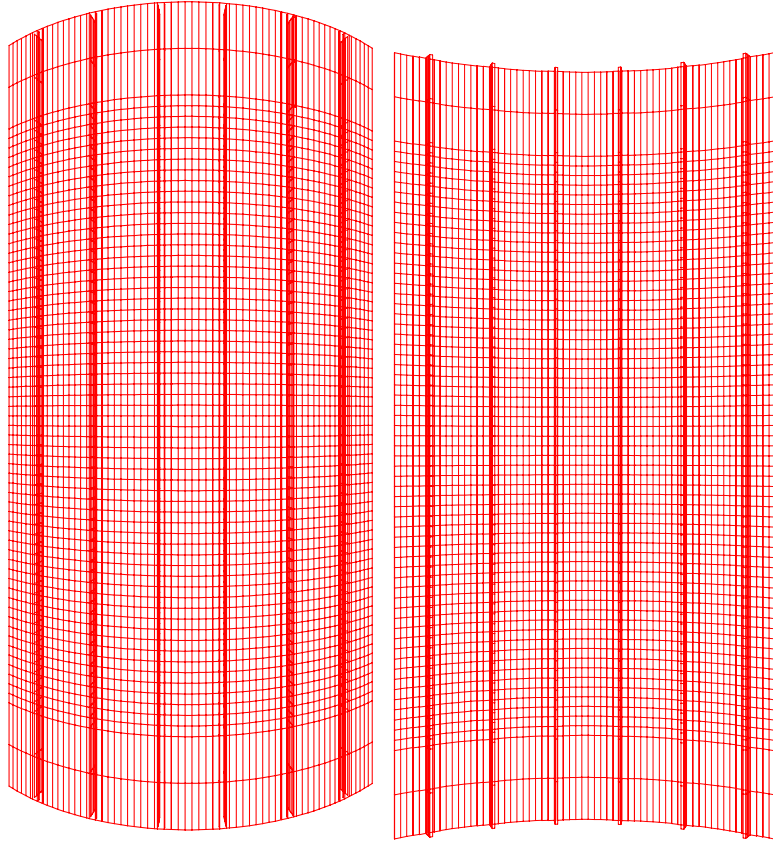
Figure 6: Discretization with Hexahedral elements

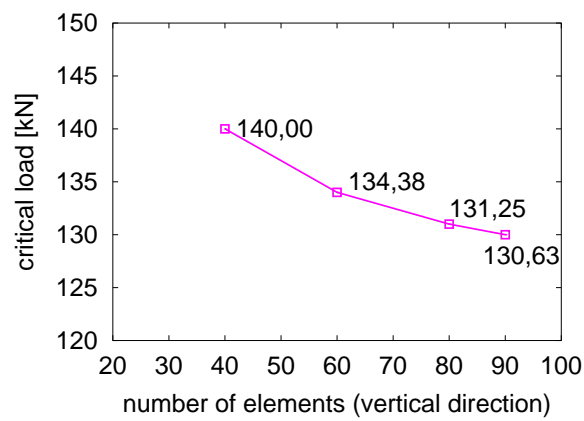| Mesh	nodes	elements
1	27318	10080
2	33582	11592
3	23142	7560
4	38734	14976

Table 3: Data of introduced FE–Hexahedral–meshes
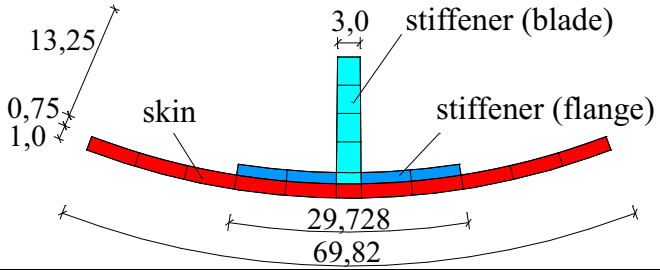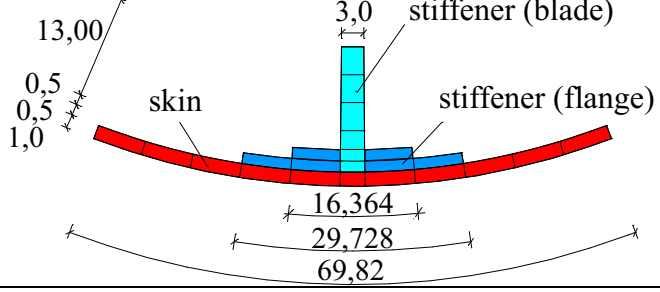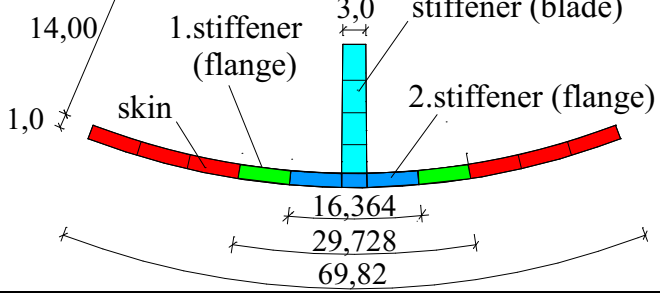

Figure 7: Critical load with respect to discretization
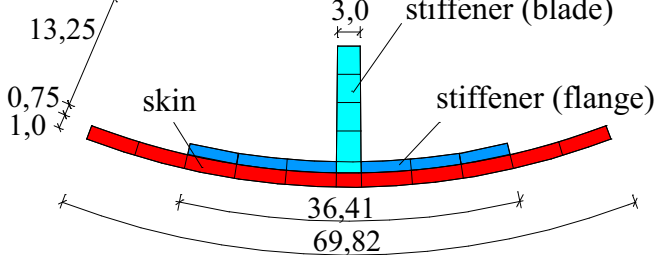
Mesh	Stringer–model	Layup in stringer base
1		$[+45, -45]_3$
2		$[+45, -45]_2$
3		$[+45, -45]_2, [+45, -45]_4$
4		$[+45, -45]_3$

Figure 8: Stringer modeling with hexahedral elements

4.3.2 Shell element

Three meshes with the following data have been chosen, see Table 4:

Mesh	nodes	elements	elements circ.	elements vertical	dofs
1	851	660	24	20+2	3407
2	2623	2268	48	40+2	12591
3	4171	3780	84	40+2	21087

Table 4: Data of introduced FE–shell–meshes

It has been tested from the hexahedral element discretization that not more than 40 elements are necessary in vertical direction to have a proper mesh. In horizontal direction 4 elements (only 2 for mesh 1) have been used for the skin between the stringers whereas the other elements are used for the stringers with different fine models. The different meshes are depicted in Fig. 9. The reference surface is the mid–surface of the skin. No imperfections have been used. The damaged areas are not discretized. The radius of the mid–surface of the cylindrical skin has been chosen to r = 370.9 mm according to [3].

The blade of the stringer is discretized with one element. The different stringer models for meshes 1–3 are depicted in Fig. 10.
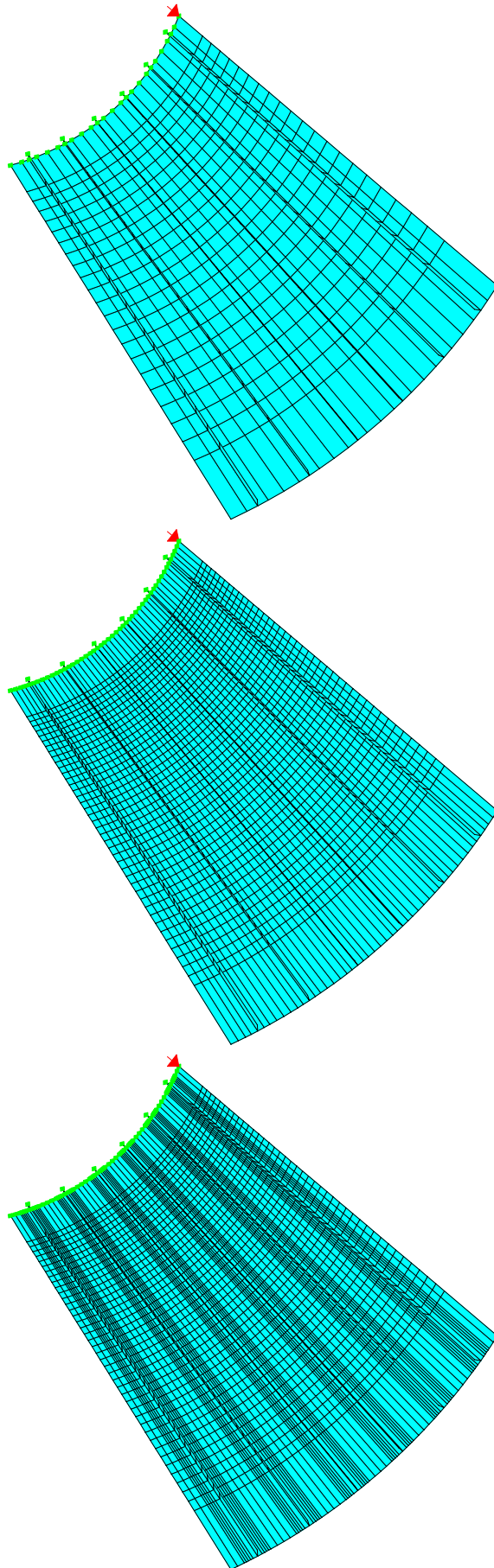
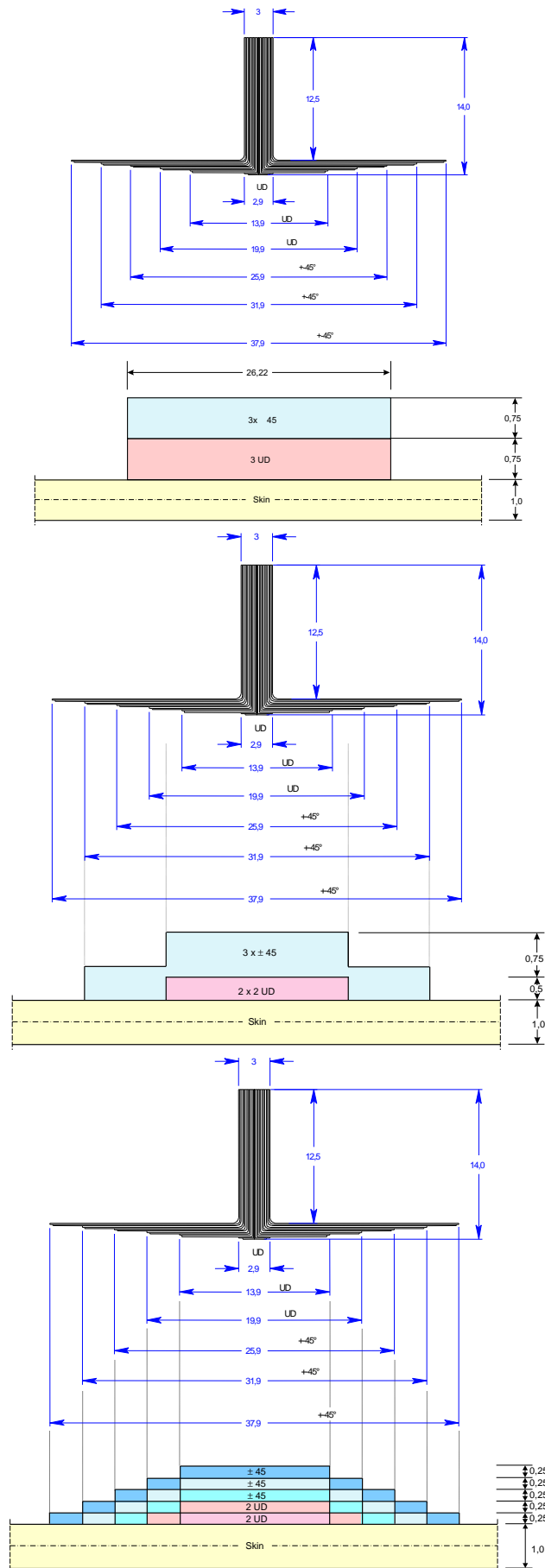Figure 9: FE–meshes with shell elements (models 1–3)

12

Figure 10: Stringer models for FE–meshes 1–3

5 Types of analyses

5.1 Solution methods

The geometrical nonlinear behaviour is calculated within several load/displacement or time steps. Solution points with an equilibrium state are found using a Newton–Raphson algorithm. All used elements have consistent tangent matrices. As a consequence quadratic convergence can be achieved. At top of the introduced meshes all nodes are linked in axial direction. Thus, the same displacement is chosen for all nodes.

Within the static analysis an arc–length procedure with arc–length control as well as displacement control has been used. An accompanying eigenvalue analysis lead to the associated nonlinear buckling loads. Furthermore linear buckling loads can be calculated.

Within the dynamic analysis an implicit Newmark–algorithm without damping has been used.

5.2 Computations

Due to the nearly linear behaviour in the prebuckling range a large load step of about 100 kN can be used. Afterwards steps were prescribed by the solution algorithm.

Dynamic algorithms are started at load level of 100 kN.

The convergence tolerance is $1 \cdot 10^{-16}$ for the energy norm within the Newton–procedure and $1 \cdot 10^{-12}$ within the eigenvalue computation via a subspace algorithm.

6 Results

6.1 Static analysis with hexahedral elements

Results of the load–deflection curves for the static analysis with hexahedral elements are depicted in Fig. 11 for the different models, defined in Fig. 8 in comparison to the experimental results [3]. For meshes 1, 2, 4 the initial stiffness of the panel is described as in the experiment. The associated buckling loads are presented in Table 5. It can be seen that the results for mesh 3, where the eccentricity of the stringer is not modeled, are not correct. Furthermore the results show that there is a rather big influence of the stringer design in the numerical model.

Mesh	nodes	elements	buckling load F_{crit} in [kN]
1	27318	10080	122.95
2	33582	11592	118.75
3	23142	7560	73.75
4	38734	14976	135.00

Table 5: Buckling loads for different hexahedral FE–meshes

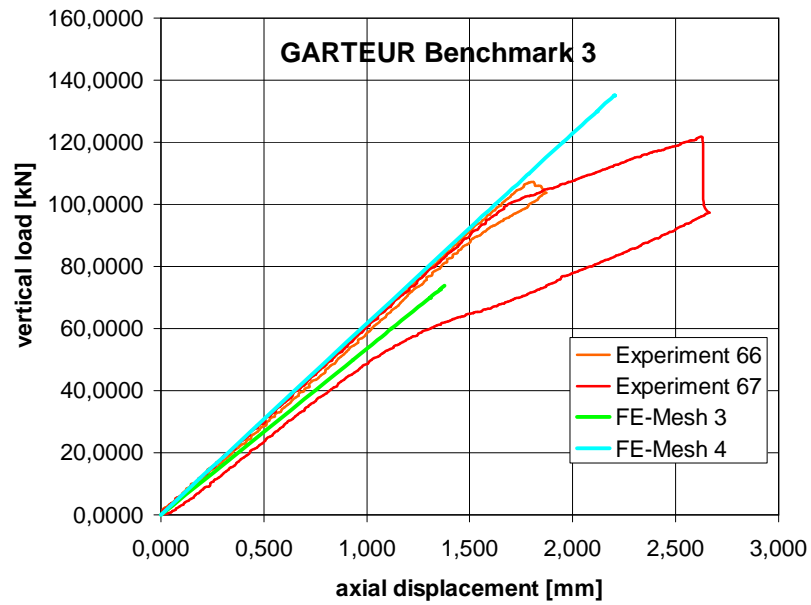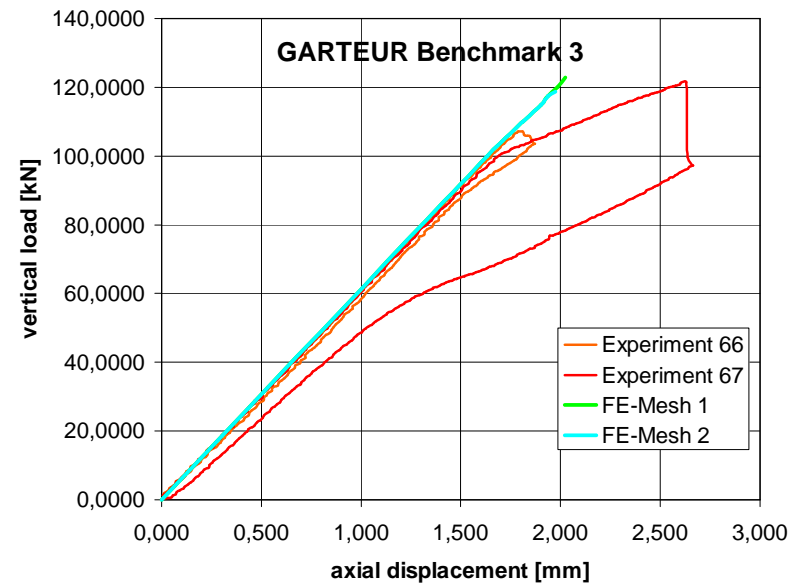The associated 1st and 2nd buckling modes are depicted in the following in Figs. 12–15.
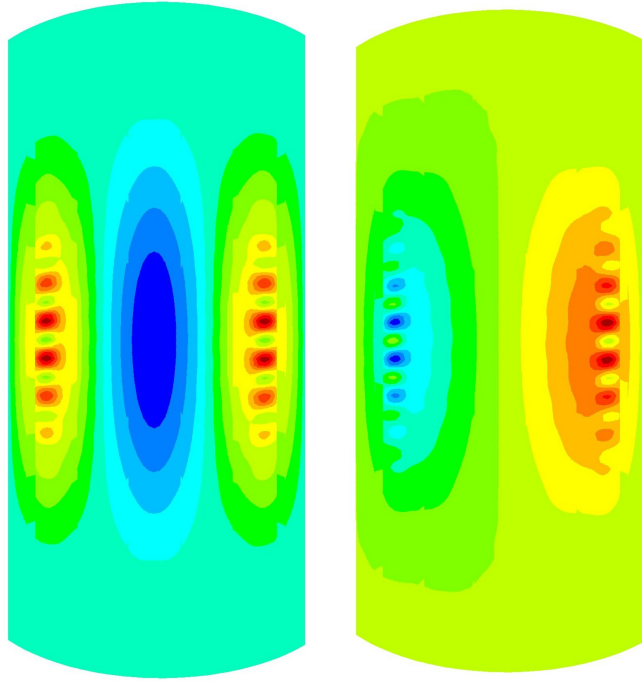
Figure 11: Load deflection curves for hexahedral–meshes 1–4

Figure 12: Hexahedral–mesh 1: 1st and 2nd buckling mode at $F_{crit} = 122.95$ kN
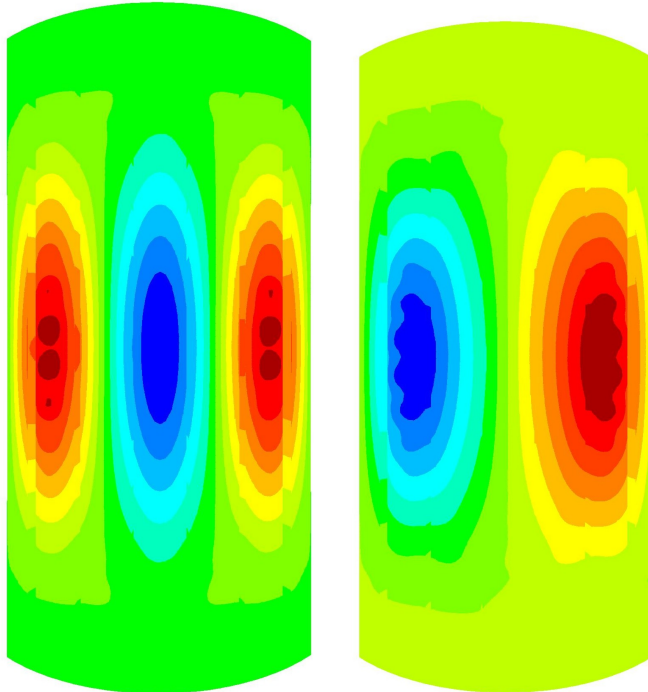

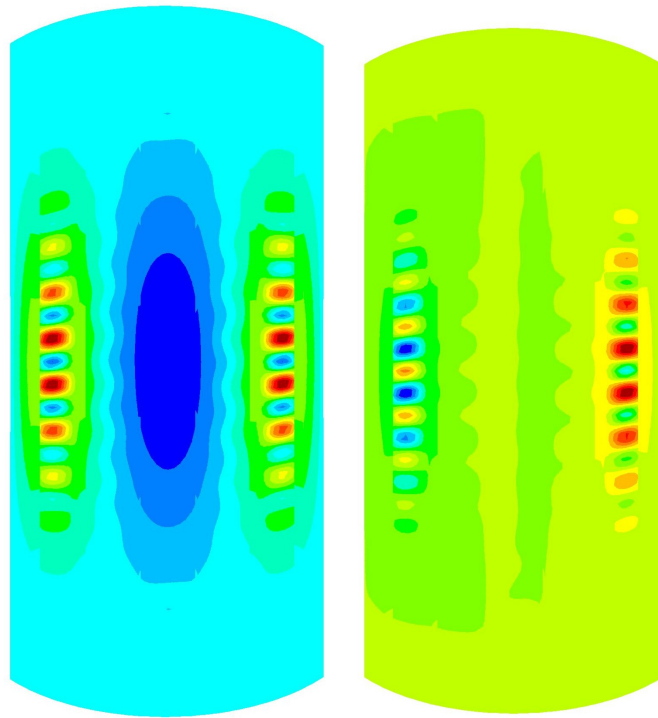Figure 13: Hexahedral–mesh 2: 1st and 2nd buckling mode at $F_{crit} = 118.75$ kN

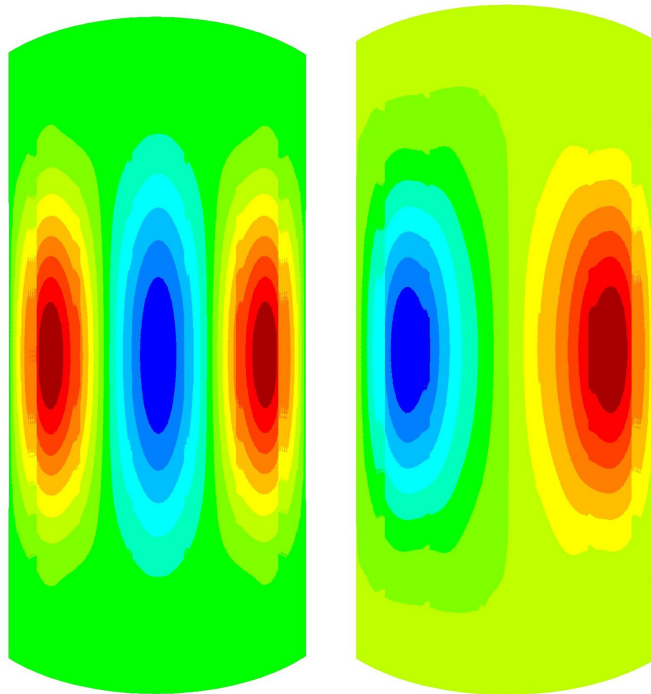Figure 14: Hexahedral–mesh 3: 1st and 2nd buckling mode at $F_{crit} = 73.75$ kN

Figure 15: Hexahedral–mesh 4: 1st and 2nd buckling mode at $F_{crit} = 135.00$ kN

16

6.2 Static analysis with shell elements

Results of the load–deflection curves for the static analysis with shell elements are depicted in Fig. 16 for the different models, defined in Fig. 9 in comparison to the experimental results [3]. The associated buckling loads are presented in Table 6. It can be seen that the course mesh 1 lead to stiff results whereas the other two meshes lead to a nearly correct behaviour.
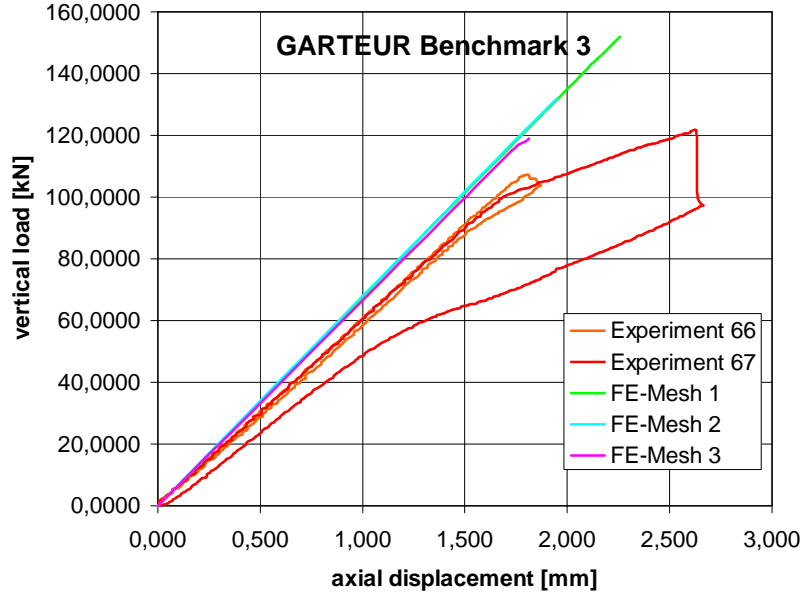

Figure 16: Load deflection curves for shell–meshes 1–3

Mesh	nodes	elements	buckling load F_{crit} in [kN]
1	851	660	152
2	2623	2268	132
3	4171	3780	119

Table 6: Buckling loads for the different shell FE–meshes

Results for mesh 1 are depicted in Figs. 17–21. Tha axial and radial displacements at the buckling point can be found in Figs. 17–18, whereas the radial displacements of the first three eigenvectors at the buckling point are presented in Figs. 19–21.

Results for mesh 2 are depicted in Figs. 22–29. Tha radial displacements at the buckling point can be found in Fig. 22. After a local buckling point, depicted in Fig. 23, the radial displacement changes to a local buckling behaviour, which can be seen in Figs. 24–25. The radial displacements of four eigenvectors at the buckling point are presented in Figs. 26–29. It can be seen that the decisive first eigenvector is now dominated by local buckling behaviour.
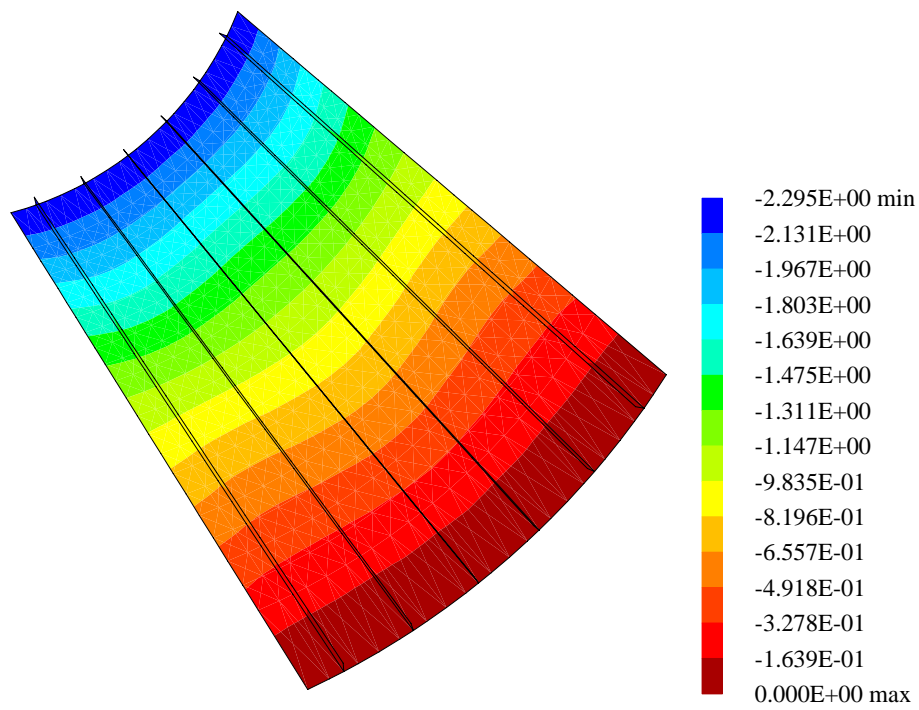
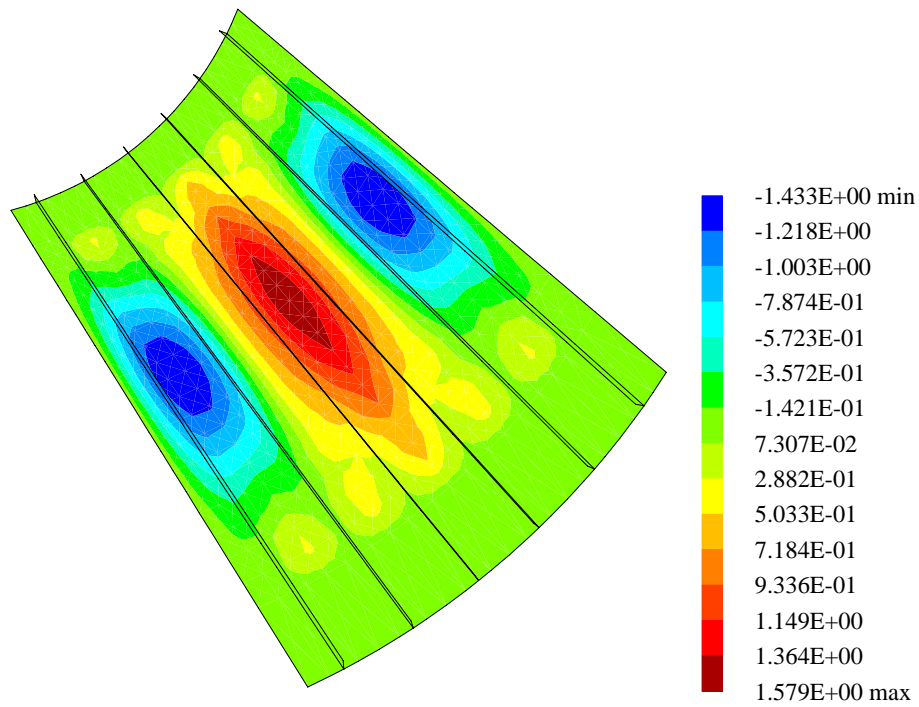Figure 17: Mesh 1: Axial displacements
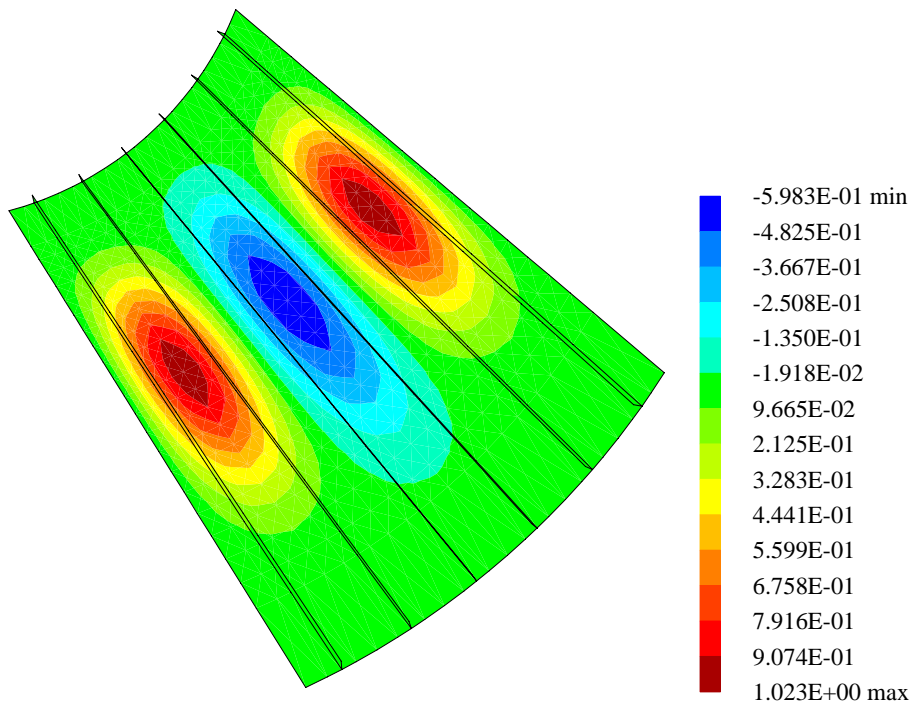

Figure 18: Mesh 1: Radial displacements

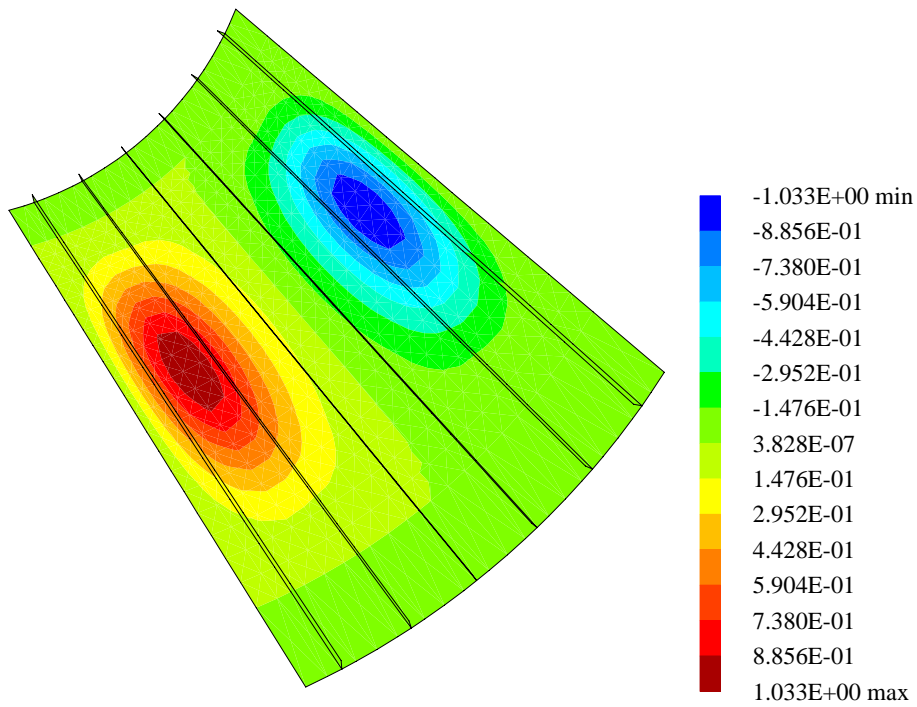Figure 19: Mesh 1: Radial displacements for eigenvector 1

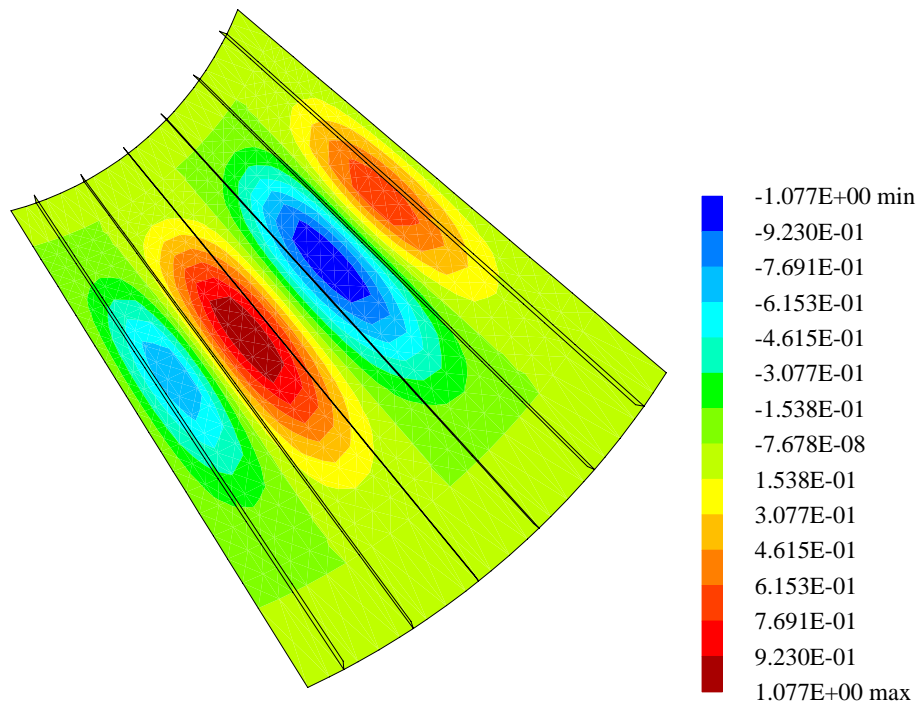Figure 20: Mesh 1: Radial displacements for eigenvector 2

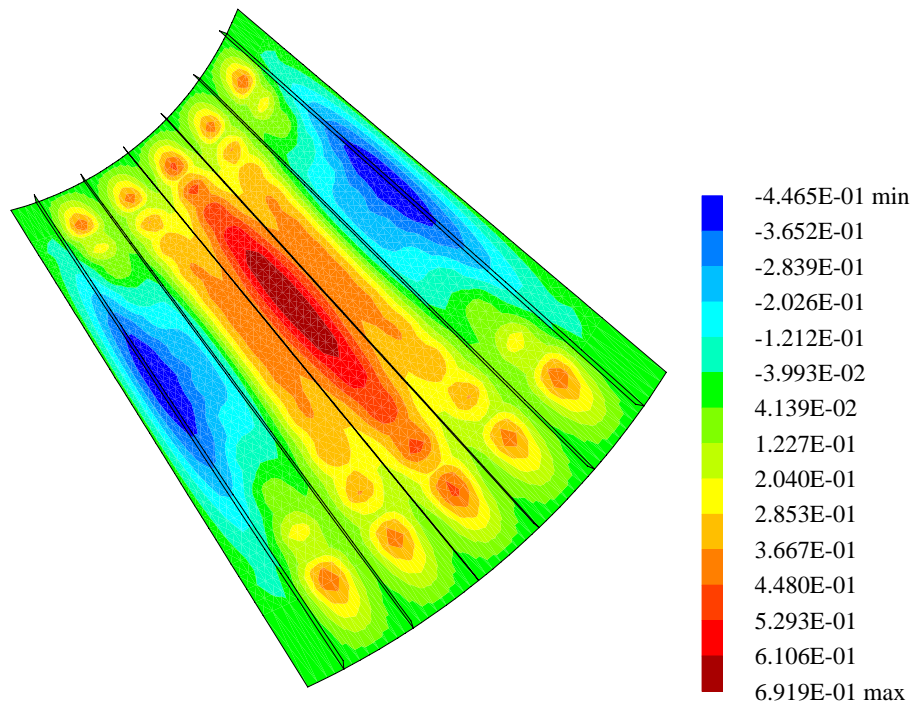Figure 21: Mesh 1: Radial displacements for eigenvector 3

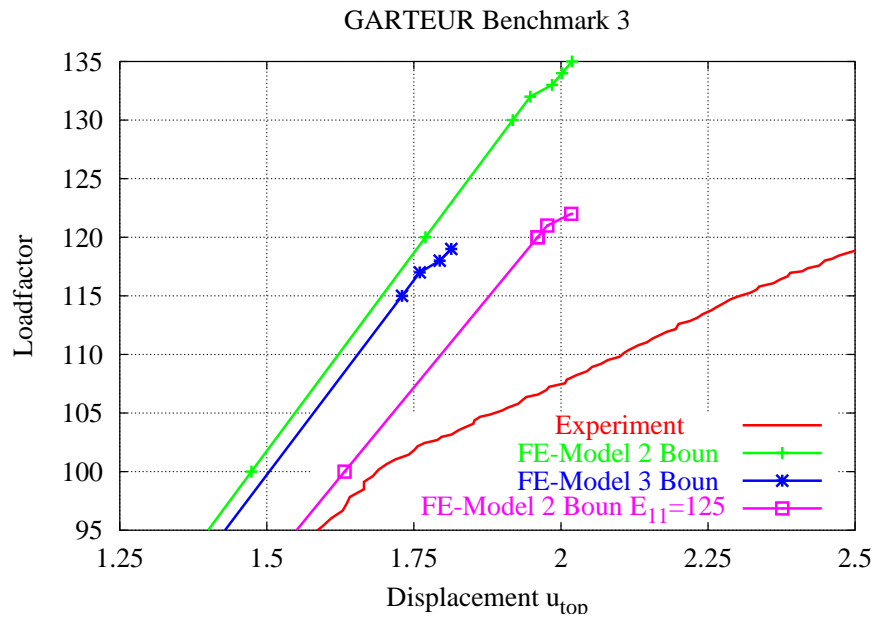Figure 22: Mesh 2: Radial displacements
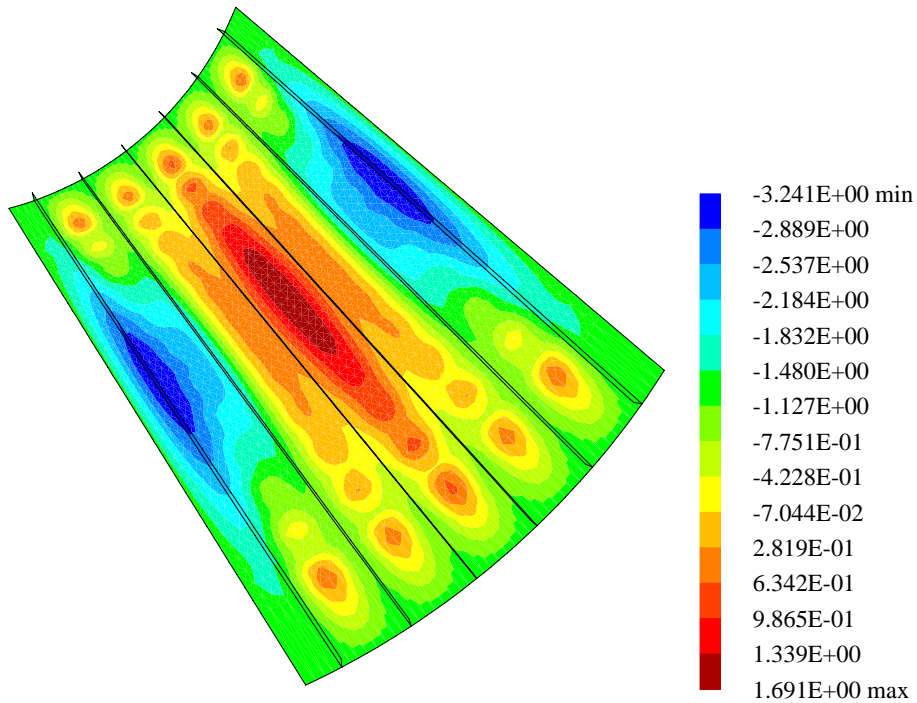
Figure 23: Mesh 2: Jump at bifurcation point

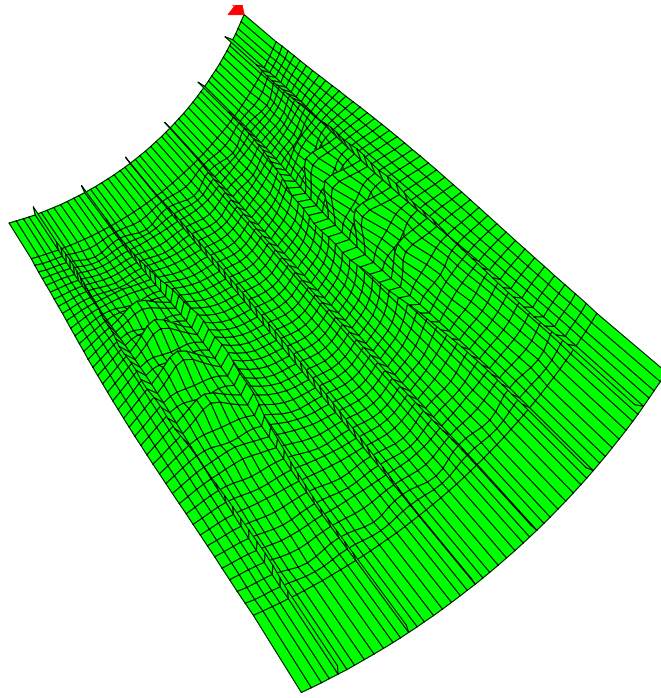Figure 24: Mesh 2: Radial displacements after local buckling

Figure 25: Mesh 2: Deformed mesh after local buckling (scale=20)

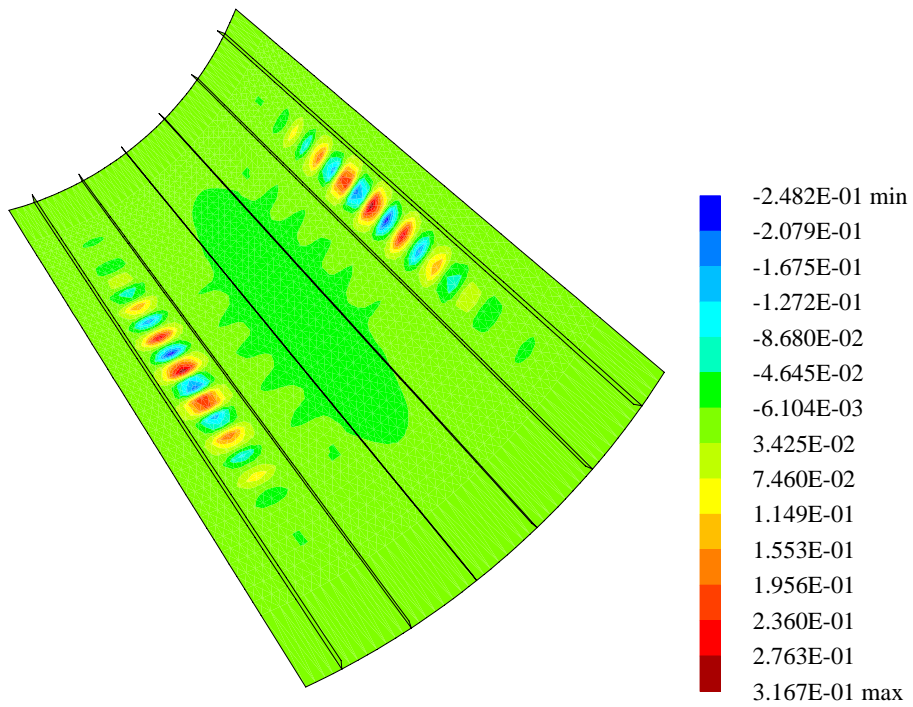| |
|---|
| -2.482E-01 min |
| -2.079E-01 |
| -1.675E-01 |
| -1.272E-01 |
| -8.680E-02 |
| -4.645E-02 |
| -6.104E-03 |
| 3.425E-02 |
| 7.460E-02 |
| 1.149E-01 |
| 1.553E-01 |
| 1.956E-01 |
| 2.360E-01 |
| 2.763E-01 |
| 3.167E-01 max |

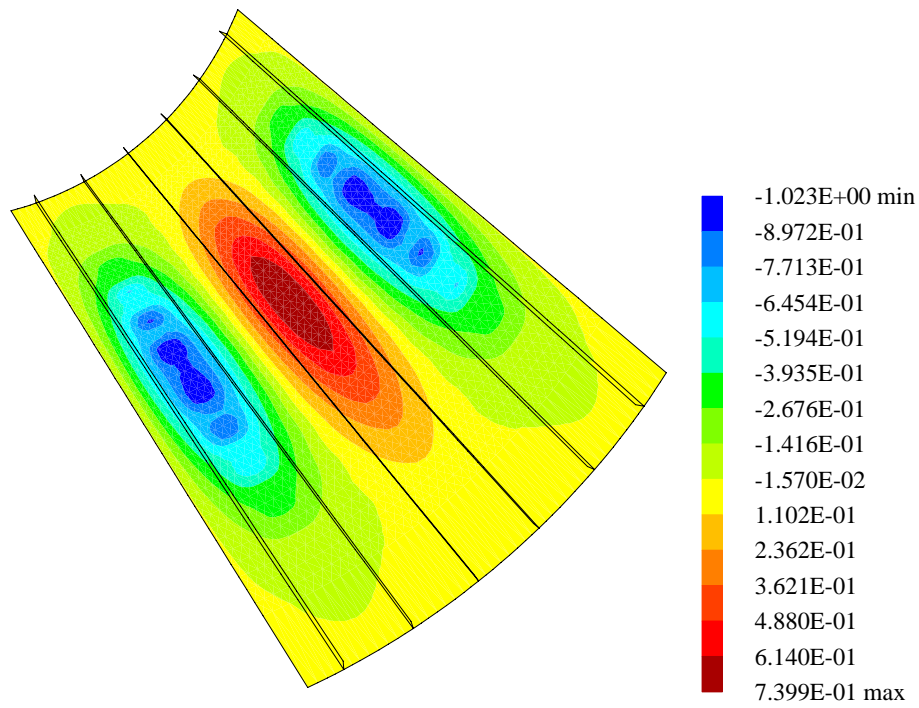Figure 26: Mesh 2: Radial displacements for eigenvector 1

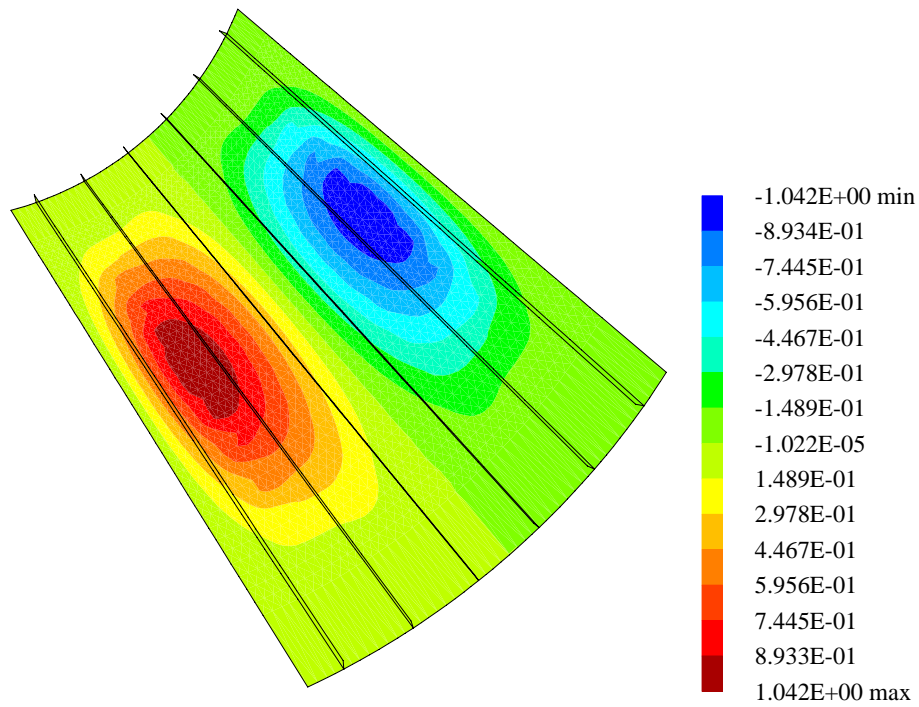Figure 27: Mesh 2: Radial displacements for eigenvector 5

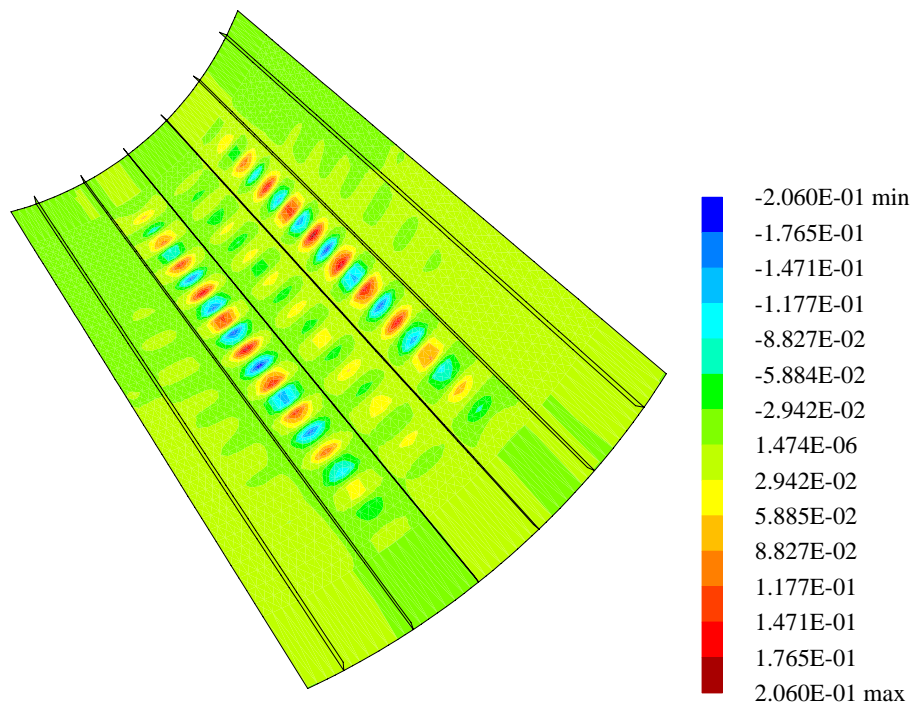Figure 28: Mesh 2: Radial displacements for eigenvector 10

23

Figure 29: Mesh 2: Radial displacements for eigenvector 11

6.3 Comparison of results from hexahedral and shell elements

Results for calculations with hexahedral and shell elements are depicted in Fig. 30. It can be seen clearly that acceptable results can be achieved with both models. It is surprising that the axial stiffness of shell models is about 10 % too high whereas the hexahedral models lead to a nearly exact behaviour. This may depend on the strong influence of the stringer models, see Figs. 8, 10. Especially for the hexahedral case coarse models have been used. Thus, the good hexhedral results may be by chance. Furthermore the mentioned element modifications may lead to a more weak element behaviour.
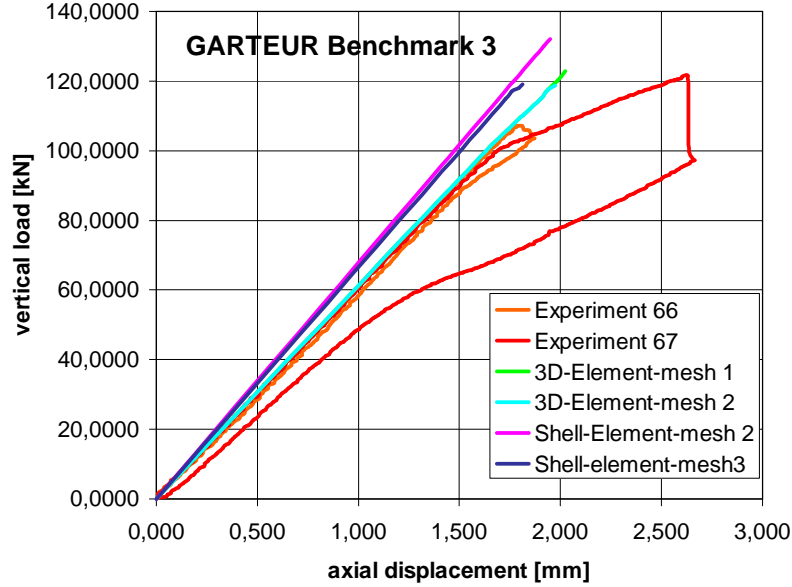

Figure 30: Load deflection curves for discretizations with hexahedral– and shell–elements

6.4 Differences in linear shell analysis

It can be seen that there exist differences in the linear axial stiffness of about 10 % between experiment and numerical analysis. These differences may depend on a certain weakness of the gypsum at the bottom of the panel in experiment. A simple numerical model may be the introduction of an elastic foundation, see Fig. 31.

The stiffness of the spring can be calculated from $c_F = \frac{E\,A}{L} = \frac{E\,U\,t}{L} = 628.38\ kN/cm$ which lead to $\tilde{c}_F = c_F/\sum_{Nodes}$. The following parameter have been chosen, see table 7.

elasticity modulus, gypsum?	E_{gypsum}	=	$3000\ N/mm^2$
length	U	=	$418.92\ mm$
thickness of skin	t	=	$1\ mm$
assumed height of boundary	L	=	$2\ mm$

Table 7: Material parameters for an assumed elastic foundation

These values may be realistic. For comparison the elastic modulus of brickwork: $E_{\text{brickwork}} =$
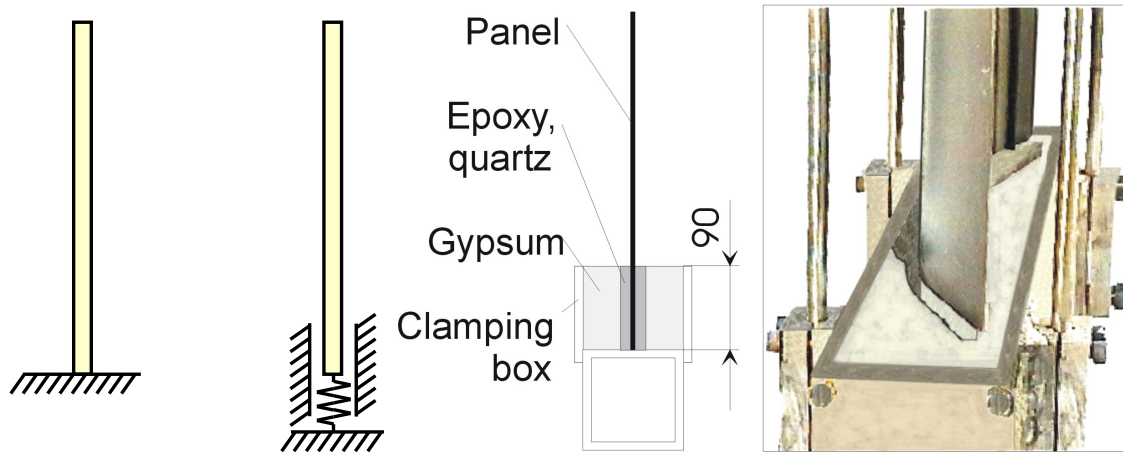
Figure 31: Elastic foundation(Spring at lower bound)

$3000 - 12000 \ N/mm^2$ is mentioned. Other possible reasons may be discussed in the report of the DLR.

6.5 Dynamic analysis with shell elements

Results for dynamic analysis are only available for calculations with shell–elements. As mentioned before an (implicit) Newmark–algorithm has been used without any numerical damping. As before no imperfections and no damage areas are incorporated in the discretization. Furthermore mesh 3 has been chosen with respect to computation time, which lead in generell to relatively stiff results, see Table 6.
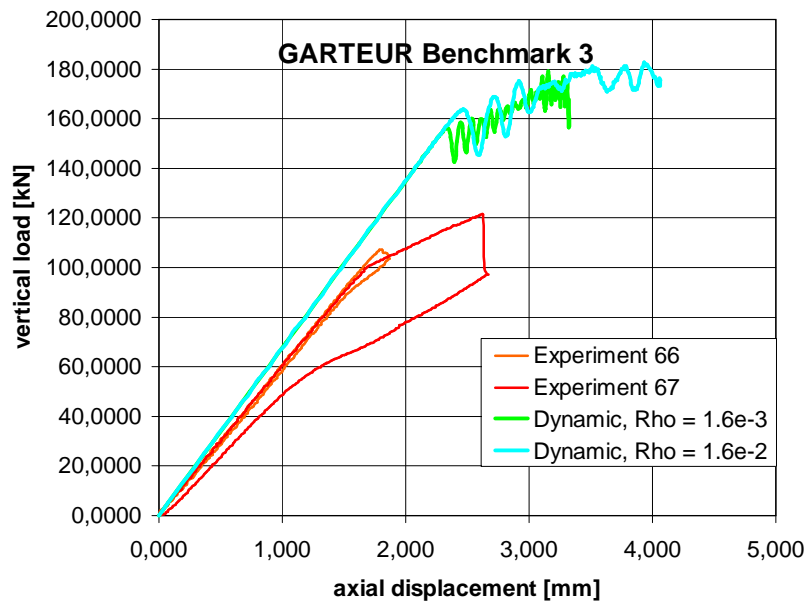

Figure 32: Load deflection curves for shell–mesh3 and different values of ρ

26

7   Conclusions

The DLR benchmark panel consists of a skin with nominally cylindrical shape, which is stiffened by stringers. The stringers are partially separated from the skin. This panel had been axially compressed until collapse. In this report numerical methods to describe the static and dynamic nonlinear behaviour of the panel have been reported. Results for calculations with hexahedral and shell elements are given. Acceptable results can be achieved with both models. These depend strongly on influence of the stringer models. The FE simulations with shell elements overestimated the initial axial stiffness by about 10 % as compared with the stiffness in the experiment whereas calculations with the hexahedral models lead to a nearly exact behaviour.

Finally, it can be stated that the FE-algorithms and -elements can be used for the simulation of the DLR benchmark. However, the nonlinear simulations required long computing times which may not be acceptable for daily design purposes in industrial applications.

References

[1] K.J. Bathe, E.Dvorkin, A Continuum Mechanics Based Four Node Shell Element for General Nonlinear Analysis, Engineering Computations, 1 (1984), 77–88.

[2] P. Betsch, E. Stein, An Assumed Strain Approach Avoiding Artificial Thickness Straining for a Nonlinear 4-Node Shell Element, Communications in Numerical Methods in Engineering, 11 (1995), 899–910.

[3] Deutsches Zentrum für Luft- und Raumfahrt e.V. (DLR) Institute of Structural Mechanics Braunschweig: Benchmark 3 of GARTEUR – AG 25 Postbuckling and Collapse Analysis: axially compressed CFRP panel

[4] J.C. Simo, M.S. Rifai, A Class of Mixed Assumed Strain Methods and the Method of Incompatible Modes, Int. J. Num. Meth. Engng., 29 (1990), 1595–1638.

[5] S. Klinkel, F. Gruttmann, W. Wagner, A continuum based 3D–shell element for laminated structures, Computers & Structures, 71, (1999), 43–62.

[6] W. Wagner, F. Gruttmann, A Simple Finite Rotation Formulation for Composite Shell Elements, Engineering Computations, 11, (1994), 145–176.

[7] O.C. Zienkiewicz, R.L. Taylor, The Finite Element Method, Vol. 2, 5th edition, Butterworth Heinemann, Oxford (2000).